



Snapshot multifocal light field microscopy

KUAN HE,^{1,*} XIAOLEI WANG,² ZIHAO W. WANG,¹  HANNAH YI,³
NORBERT F. SCHERER,^{2,3} AGGELOS K. KATSAGGELOS,⁴ AND
OLIVER COSSAIRT¹

¹Department of Computer Science, Northwestern University, 633 Clark St, Evanston, IL 60208, USA

²James Franck Institute, The University of Chicago, 5801 South Ellis Avenue, Chicago, IL 60637, USA

³Department of Chemistry, The University of Chicago, 5801 South Ellis Avenue, Chicago, IL 60637, USA

⁴Department of Electrical and Computer Engineering, Northwestern University, 633 Clark St, Evanston, IL 60208, USA

*hekuan625@gmail.com

Abstract: Light field microscopy (LFM) is an emerging technology for high-speed wide-field 3D imaging by capturing 4D light field of 3D volumes. However, its 3D imaging capability comes at a cost of lateral resolution. In addition, the lateral resolution is not uniform across depth in the light field deconvolution reconstructions. To address these problems, here, we propose a snapshot multifocal light field microscopy (MFLFM) imaging method. The underlying concept of the MFLFM is to collect multiple focal shifted light fields simultaneously. We show that by focal stacking those focal shifted light fields, the depth-of-field (DOF) of the LFM can be further improved but without sacrificing the lateral resolution. Also, if all differently focused light fields are utilized together in the deconvolution, the MFLFM could achieve a high and uniform lateral resolution within a larger DOF. We present a house-built MFLFM system by placing a diffractive optical element at the Fourier plane of a conventional LFM. The optical performance of the MFLFM are analyzed and given. Both simulations and proof-of-principle experimental results are provided to demonstrate the effectiveness and benefits of the MFLFM. We believe that the proposed snapshot MFLFM has potential to enable high-speed and high resolution 3D imaging applications.

© 2020 Optical Society of America under the terms of the [OSA Open Access Publishing Agreement](#)

1. Introduction

Light field microscopy (LFM) offers a single-shot, three-dimensional (3D) imaging since its invention in 2006 [1]. Unlike a conventional wide-field microscope where a two-dimensional (2D) image representing the spatial distribution of the focal plane of the 3D volumes is recorded, the LFM simultaneously collects both the spatial and angular information (so-called 4D light field) of the volumes. This incredible capability is achieved by placing a microlens array (MLA) at an intermediate image plane, where an image sensor would originally be positioned for a conventional microscopy. The sensor itself is moved back so that it focuses on the rear focal plane of the MLA to capture the light field of the 3D volumes. The number of pixels $N_u \times N_v$ behind each lenslet determines angular resolution of the LFM. This angular resolution is what allows 3D volumetric reconstructions in the LFM and determines its depth-of-field (DOF), which can be expressed as [1,2]:

$$\text{DOF}_{\text{LFM}} \approx \frac{(2 + N_u^2)\lambda n}{2\text{NA}^2}, \quad (1)$$

where λ is the wavelength of the light, n is a refractive index, and NA is numerical aperture of microscopic objective lens. Here we assume that $N_u = N_v$. Note that a conventional microscope can be considered as a special case of the LFM where $N_u = N_v = 1$. Schematic diagrams of the conventional microscope and LFM optical setups are illustrated in Figs. 1(a) and 1(b), respectively.

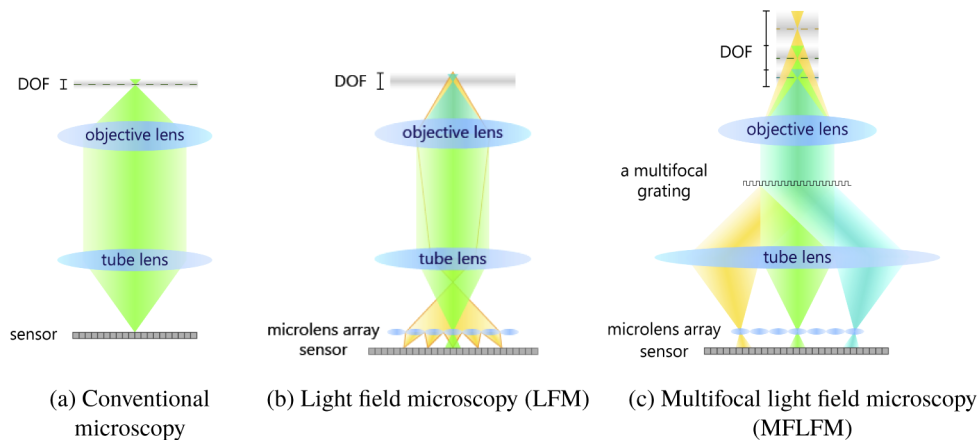


Fig. 1. Schematic diagrams comparison between (a) a conventional microscopy, (b) LFM and (c) proposed MFLFM. The LFM (b) records light field of 3D volumes by placing a microlens array in front of a sensor. The MFLFM (c) simultaneously collects multiple light fields by placing a multifocal grating at the Fourier plane of the system. Each light field has its corresponding focal plane in the volume.

For the light field processing, there are two common algorithms: ray-optics based synthetic focusing algorithms [1,3] and wave-optics based deconvolution algorithms [4]. Unfortunately, both algorithms suffer from several limitations:

- **A trade-off between lateral resolution and DOF in synthetic focusing reconstructions.** Synthetic focusing algorithms use the captured light field to compute a sequence of images focused at different depths. Consequently, an instant focal stack of the 3D volumes can be generated. However, this focal stack suffers from low pixel and optical lateral resolution. The loss of the lateral resolution is exactly proportional to the gain of the angular resolution. Therefore, a larger DOF with a higher angular resolution comes at the cost of the lower lateral resolution. This is an inherent trade-off in the conventional LFM system design and synthetic focusing algorithms alone cannot eliminate it unless a different light field system is introduced. For instance, a hybrid light field imaging [5] that includes a light field camera and a regular camera was recently proposed to improve spatial lateral resolution. Another example is utilizing a lenslet array with non-uniform focal lengths and aperture sizes [6,7] to enlarge DOF in the light field macroscopic imaging.
- **Non-uniform lateral resolution across depth in the light field deconvolution reconstructions.** A light field deconvolution algorithm [4] was introduced to improve the spatial lateral resolution of the LFM. It relies on the knowledge of the light field point spread functions (PSFs) and a wave-optics optical model for the LFM, and is able to reconstruct volumes with resolution finer than the lenslet spacing. However, as was shown in [4], the achievable lateral resolution of the LFM deconvolution is not uniform across depth: the lateral resolution decreases linearly with increasing z depth from moderate to large z positions due to evolution of the sampling density with depth.
- **No lateral resolution improvement at the center of imaged volumes in the light field deconvolution reconstructions.** Previous work [4] also showed that the resolution enhancement at the center of the volumes cannot be achieved even with light field deconvolution algorithms for the LFM. This is because the spatial sampling density at the native focal plane is sparse that deconvolution algorithms cannot allow super-resolution.

Recently, a wavefront coding technique [8] by placing phase masks in the optical path was introduced to improve the poor resolution at the native focal plane for the LFM.

To address all three above limitations of the LFM, in this paper, we propose a novel snapshot multifocal light field microscopy (MFLFM) imaging system as illustrated in Fig. 1(c). The underlying concept of the MFLFM is collecting multiple focal shifted light fields simultaneously, with each light field focusing at different z depths in the object space. By focal stacking those focal shifted light fields, the DOF of the LFM can be further improved but without sacrificing its lateral resolution. In addition, if used together with light field deconvolution algorithms, the MFLFM could mitigate the non-uniform lateral resolution problem across depth of the LFM, and also achieve resolution enhancement at the center of imaged volumes. To realize the MFLFM, we designed a multifocal grating (MFG) and placed it at the Fourier plane of a conventional LFM. The physical model and optical performance of the proposed MFLFM are derived and given. Both simulations and proof-of-principle experimental results are provided to demonstrate the effectiveness and benefits of the MFLFM.

The paper is organized as follows: in Section 2 we describe the principle and system designs for the MFLFM. The extended DOF and theoretical lateral resolution limits for the MFLFM are derived and given. In Section 3, we present a house-built MFLFM imaging system prototype by using our designed and manufactured MFG. We show experimental PSFs of the MFLFM to validate its capability of recording 9 focal shifted light fields in a snapshot without a need of focal scanning. We also experimentally demonstrate a $8\ \mu\text{m}$ DOF improvement of the MFLFM over the LFM by using synthetic focusing algorithms for the light field reconstructions. In addition, we present numerical simulations using a USAF 1951 resolution test target to demonstrate a higher and more uniform lateral resolution reconstructions in the MFLFM light field deconvolution. Finally, the conclusion and discussion are given in Section 4.

2. Principle and optical performance of the MFLFM

2.1. Principle and system designs of the MFLFM

Multifocal imaging is commonly implemented by either splitting the light path with prisms and imaging with multiple sensors focused at different depths in the volumes [9–11] or employing an MFG at the Fourier plane of a conventional microscope [12,13]. Likely, there are two different implementations of the MFLFM system depending on whether utilizing an MFG or not. In this paper, we built an MFLFM system by placing an MFG at the Fourier plane of a conventional LFM, but the analysis and conclusions presented here are applicable to both MFLFM implementations. As illustrated in Fig. 1(c), an MFG is placed at the Fourier plane of the LFM. The MFG has two roles: first, it splits the light onto different diffraction directions. As a consequence, the rays are separated and distributed on the different regions of the MLA. Second, it introduces order-dependent focusing distances: different diffraction order light focuses at different distances in the object space. Therefore, after those rays passing through the MLA and propagating to the sensor plane, the order-dependent focal shifted light fields can be simultaneously collected at different regions of the sensor in one exposure time. The focal shift distance Δz between two adjacent light fields and the number of collected simultaneous focal shifted light fields N are pre-determined in the MFG design phase. There are two considerations in choosing the value of N . First, it defines a trade-off between simultaneously captured focal-planes number and lateral field-of-view (FOV). Second, it affects the diffraction efficiency of the MFG. In general, the higher N is, the higher the total diffraction efficiency of a binary phase grating is, but the lower the average diffraction efficiency per focal plane. The theoretical diffraction efficiency of the grating can be improved with more number of phase steps [14], but each step level makes fabrication of devices more challenging. The most commonly used number for N is 3×3 [12–15] or 5×5 [16] in the literature. In this paper, we designed and fabricated a binary phase grating

with a 3×3 focal shifts for a proof-of-concept demonstration of proposed MFLFM system. The more details on the MFG design and fabrication process are available in Appendix C of [13].

2.2. Extended depth-of-field of the MFLFM

The MFLFM is able to increase DOF of the LFM by focal stacking differently focused light fields. If the focal shift distance Δz is equal or smaller than a DOF of a single light field, the MFLFM increases DOF of the LFM by $(N - 1)\Delta z$. Therefore, the DOF of the MFLFM can be expressed as:

$$\text{DOF}_{\text{MFLFM}} = \text{DOF}_{\text{LFM}} + (N - 1)\Delta z, \quad (2)$$

where DOF_{LFM} is given in Eq. (1). By comparing Eqs. (1) and 2, we can see that the MFLFM is able to increase the DOF of the LFM by increasing N or Δz instead of increasing the angular resolution of the light field, which would in turn decrease the lateral resolution. Therefore, if synthetic focusing algorithms are used to reconstruct 3D volumes, the MFLFM permits a larger DOF than the LFM but without further sacrificing the lateral resolution. The implementation details of the synthetic focusing algorithms on the MFLFM light fields reconstruction will be discussed in section 3.2 where experimental results are demonstrated.

2.3. Uniform lateral resolution across depth of the MFLFM

As mentioned previously, light field deconvolution algorithms rely on the physical model of the imaging system. The forward model for the MFLFM is similar to the LFM [4]:

$$g(x, y) = \sum_{u=1}^{N_u} \sum_{v=1}^{N_v} \sum_{z=1}^{N_z} [h^{u,v}(x, y; z) * f^{u,v}(x, y; z)], \quad (3)$$

where (u, v) denote pixel coordinate behind each lenslet, $h^{u,v}(x, y; z)$ denotes spatially varying (or sub-aperture) PSFs of the MFLFM, $*$ denotes a 2D convolution operator in x - y dimensions, and $f^{u,v}(x, y; z)$ is a sub-sampled version of the 3D image. For simplicity, Eq. (3) can be rewritten in a matrix-vector multiplication form:

$$\mathbf{g} = \mathbf{H}\mathbf{f}, \quad (4)$$

where \mathbf{g} and \mathbf{f} are vectorized forms of $g(x, y)$ and $f^{u,v}(x, y; z)$ respectively, and \mathbf{H} is a measurement matrix constructed from PSFs $h^{u,v}(x, y; z)$. For the light field deconvolution reconstruction, the following cost function based on a Poisson noise model is minimized [4]:

$$\min_f \sum_{i=1}^N \{(\mathbf{H}\mathbf{f})_i - \mathbf{g}_i \log[(\mathbf{H}\mathbf{f})_i]\}, \quad (5)$$

where i denotes pixel index. This objective is solved using Richardson-Lucy (RL) deconvolution algorithms [4].

Here, we demonstrate that if used together with the light field deconvolution algorithms as described above, the MFLFM could mitigate the non-uniform lateral resolution problem of the LFM deconvolution. In addition, the MFLFM could also improve the lateral resolution at the center of the imaged volume where the LFM deconvolution fails. To this end, we derive the theoretically achievable lateral resolution limits for the MFLFM. As was shown in [4], the theoretical lateral resolution limits for the LFM where a light field is focusing at the native focal plane is expressed as:

$$R_{\text{LFM}}^{\text{xy}}(z) = \frac{0.94\lambda M|z|}{d}, \quad |z| \geq \frac{d^2}{2\lambda M^2}, \quad (6)$$

where M is the magnification of the imaging system and d is a lenslet spacing. Since the MFLFM collects N focal shifted light fields, the lateral resolution at z depth would always be the highest

lateral resolution among those N light fields. This leads to an expression for the lateral resolution limits in the MFLFM:

$$R_{\text{MFLFM}}^{\text{xy}}(z) = \max_k R_{\text{LFM}}^{\text{xy}}(z - k\Delta z), \quad 1 \leq k \leq N, \quad (7)$$

where $R_{\text{LFM}}^{\text{xy}}(z - k\Delta z)$ is the theoretical lateral resolution limits for the k -th light field focusing at the $k\Delta z$ depth collected in the MFLFM.

From Eq. (6), one can see that the lateral resolution in the LFM deconvolution reconstructions is not uniform across depth. The maximum resolution is achieved at $z = \pm z_c$ depths where $z_c = d^2/(2\lambda M^2)$, and then it linearly decreases with increasing z positions. On the other hand, for the MFLFM, the maximum lateral resolution can be achieved at multiple depths whose $z = k\Delta z \pm z_c$ where $1 \leq k \leq N$. In addition, the center of the volumes can also achieve a higher lateral resolution or even maximum resolution if Δz is chosen such that $k\Delta z \pm z_c = 0$. To illustrate this, the theoretical lateral resolution limits computed from Eqs. (6) and 7 are shown in Fig. 2. It can be seen that the theoretical lateral resolution for the MFLFM deconvolution reconstructions (blue) is more uniform across depth than that of the LFM (red).

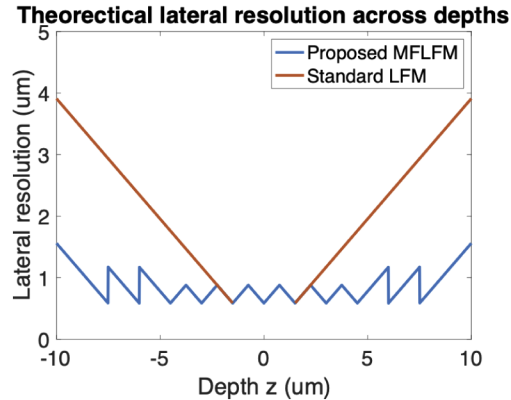


Fig. 2. The theoretical lateral resolution limits across depth (horizontal axis) for the LFM (red) and MFLFM (blue) computed from Eqs. (6) and 7. Note that there is no theoretical lateral resolution prediction in Eq. (6) for the depths near the center of the imaged volumes (around $z = 0\mu\text{m}$) for the LFM (red line). We assumed green light ($\lambda = 0.52\mu\text{m}$), a magnification of 120, and a lenslet spacing of $150\mu\text{m}$. We also assumed a total of 9 light fields with a focal shift of $1\mu\text{m}$ was collected in the MFLFM, which was the same as in our experiment and simulation shown in Section 3.

3. Experimental and simulation results

In this section, we present experimental and simulated results that demonstrate the effectiveness and benefits of the MFLFM. We begin with experimental results using our house-built MFLFM imaging system. In section 3.1 we describe the experimental setup of our MFLFM and in section 3.2 we show the captured PSFs and experimental reconstructions of the MFLFM. We experimentally demonstrate an extended DOF over the LFM when the synthetic focusing algorithms are used for the light field reconstructions. In section 3.3 we show simulation results of light field deconvolution reconstructions for both LFM and MFLFM using a USAF 1951 resolution test target. The quantitative comparisons were performed to show that the MFLFM permits a deconvolution reconstructions with a more uniform lateral resolution than the LFM.

3.1. Experimental setup

A schematic of our MFLFM imaging system is shown in Fig. 3. It consists of three main components: (1) a conventional microscope, (2) a multifocal grating (MFG), and (3) an MLA. First, a conventional fluorescence microscopy (Nikon Eclipse Ti) with an objective lens (Nikon 60x 1.27 NA CFI Plan Apo water immersion, MRD07650), a dichroic filter ((Semrock, FF596-Di01-25x36)), and a tube lens is used to collect fluorescence light emitted from a 3D sample. The excitation light is bandpass filtered (Semrock FF01-578/21-25) from a solid-state LED light source (Lumencor, Spectral X light engine). In order to avoid the overlapping between differently focused light fields, a field stop is placed at the intermediate image plane, which crops the image plane to $2 \times 2 \text{ mm}^2$ for the MFLFM. The field stop consisted of a 200 nm Cr layer with a 2 mm square clear region deposited on a circular 25.4 mm diameter by 1 mm thick fused silica substrate (Thorlabs WG41010). Second, an MFG is placed in the Fourier plane of a relay lens system (Thorlabs AC508-200-A; Thorlabs AC508-400-A) to diffract different depths of the 3D sample onto different diffraction order directions. To mitigate the dispersion of the grating, a narrow band pass filter (Semrock, FF01-620/14-25) is placed just behind the MFG, which is not plotted here. Finally, an MLA (Thorlabs, MLA150-7AR) and an electron-multiplying charge-coupled device (EMCCD, Andor iXon Ultra 888) sensor are used together to capture the light fields. Figure 4 show our house-built prototype of the MFLFM: a conventional fluorescence microscope [(a)], the MFG optics [(b)], and the MLA and EMCCD [(d)] respectively.

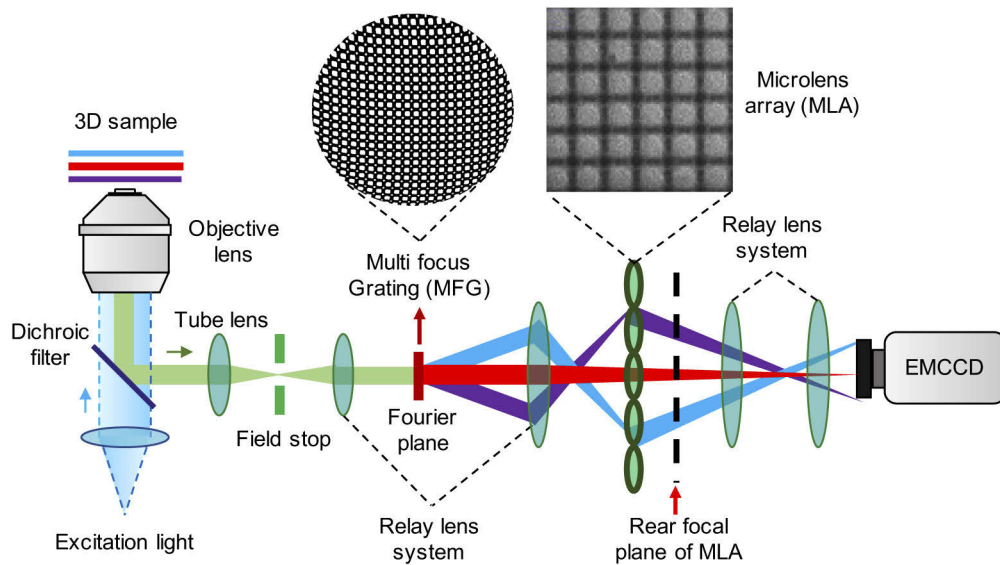


Fig. 3. Schematic of single-shot 3D MFLFM. An MFG is placed at the Fourier plane of the first relay lens system to separate and focus different depths of a 3D sample onto different diffraction orders, which later propagate through different sub-regions of the MLA and form differently focused light fields on the EMCCD sensor in a single shot. The insets show the patterns of the MFG and lenslet in the array.

To ensure that the EMCCD sensor is properly focusing at the rear focal plane of the MLA and captures light fields properly, we performed two-step calibrations for our MFLFM system. First, we illuminated the MLA with a collimated light and captured a sharp image of the MLA. This step ensured that the EMCCD sensor plane is conjugated with the MLA plane. Second, we slowly increased the EMCCD-to-MLA distance until a diffraction-limited focusing spot was

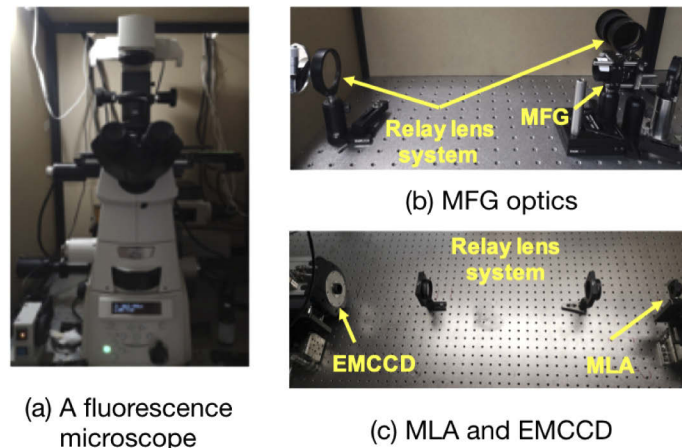


Fig. 4. A house-built MFLFM prototype: (a) a conventional fluorescence microscope, (b) the MFG optics, and (c) an MLA and EMCCD.

formed behind each microlens, which indicated that the EMCCD sensor was correctly focusing on the rear focal plane of the MLA.

In our proof-of-principle MFLFM experiment, the fluorescence emission light had a wavelength of $0.61 \mu\text{m}$. The lenslet spacing in the array is $150 \mu\text{m}$ and each lenslet has a diameter of $146 \mu\text{m}$ and a focal length of 5.2 mm . The EMCCD sensor has 1024×1024 pixels with a pixel pitch of $13 \times 13 \mu\text{m}^2$. The MFG was designed to be able to generate 3×3 differently focal shifted light fields with a total diffraction efficiency of 68% . The focal shift Δz between adjacent light fields was $1 \mu\text{m}$, which corresponded to about $8 \mu\text{m}$ improvement in the DOF over the LFM according to the theory of Eq. (2).

3.2. Experimental results with extended depth-of-field

To validate the MFLFM system, we captured the PSFs by imaging a sub-resolution (200 nm diameter) fluorescent bead at different z positions using our MFLFM system. For comparison, the PSFs of a conventional LFM were also captured. We can see the MFLFM [Fig. 5(b)] was able to collect 3×3 focal shifted light fields simultaneously compared to the LFM [Fig. 5(a)]. By tracking the focused light field tile with depth, the focal shift between two adjacent light field tiles could be estimated.

To experimentally demonstrate extended DoF of MFLFM over the LFM, we imaged 6 fluorescence beads using both MFLFM and LFM imaging systems. Each bead has a 3D size of $4 \times 4 \times 4 \mu\text{m}^3$. 4 out of 6 beads were located at depth $z = 0 \mu\text{m}$, while the other 2 beads were located at depth $z = 3 \mu\text{m}$. We collected a series of the light field measurements as the 3D volume was translated to different z -heights. An example of a snapshot captured MFLFM light fields is shown in Fig. 6(a). Like its PSFs as shown in Fig. 5(b), the MFLFM measurement also consisted of 9 light fields with each light field having its corresponding focal plane in the object space. For the MFLFM light field processing, we first applied synthetic focusing algorithms to each individual light field independently. Then, we fused 9 focal stacks generated from each light field. The center offset between different focal stacks can be pre-estimated from the MFLFM PSFs. The 3D volumetric reconstructions from the synthetic refocusing algorithms for the LFM (top row) and MFLFM (bottom row) are shown in Fig. 6(b). To quantitatively analyze the reconstruction quality, a 2D slice of the 3D reconstructed volumes are shown in Figs. 6(d) and (e) for the LFM and MFLFM, respectively. Each 2D slice was refocusing at the z -position of the three beads in a red dash rectangle. In addition, the wide-field microscopy images of the same scene are shown in

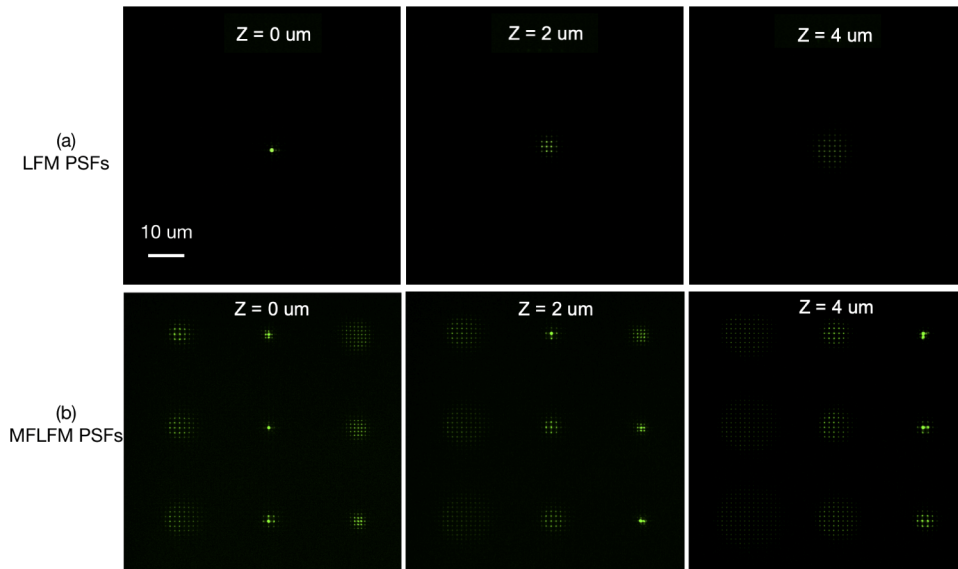


Fig. 5. Comparison of experimental PSFs of a conventional LFM (a) and the MFLFM (b) by imaging a sub-resolution (200 nm) fluorescent bead at different z-positions (columns). It demonstrates that the proposed MFLFM system is able to capture 9 differently focused light field in a single shot. The scale bar denotes the length in the object space.

Fig. 6(c). The linecuts comparisons indicated by solid red lines in the rectangle for three imaging methods are also plotted in Figs. 6(f-h), respectively. As expected, a wide-field microscopy could produce a high resolution image when the centers of three beads were located at the native focal plane $z = 0 \mu\text{m}$ [first column in (c) and (f)]. However, the images of three beads became much blurrier as the sample were translated further away from the focal plane [second to last columns in (c) and (f)]. The LFM could enable post-capture digital refocusing of the three beads until to the $z = -6 \mu\text{m}$ position [middle column in (d) and (g)], beyond which the spatial resolution of the LFM refocused image decreased and three beads could not resolved by the LFM (last two columns). From Figs. 6(e) and (h), we can see that the three beads could be well separated from $z = 0$ until $z = -10 \mu\text{m}$ in the proposed MFLFM light field refocusing. The experimental results shown in Fig. 6 demonstrated that the MFLFM could increase the DOF of the LFM by $4 \mu\text{m}$ in the direction below the native focal plane. The reconstruction quality appeared similar as the 3D volume was translated up above the native object plane. Therefore, a total of $8 \mu\text{m}$ DOF improvement over the LFM was achieved in our MFLFM proof-of-principle experiment, which was consistent with the theoretical predication as calculated from Eq. (2) in Section 3.1.

3.3. Simulated results with uniform lateral resolution across depth

In this section, we present simulation results of the MFLFM light field deconvolution to demonstrate its uniform lateral resolution within the DOF. In the simulation, we used a USAF 1951 resolution test target of 187×187 pixels [shown in Fig. 7(a)] as a ground truth. The partially spatial varying PSFs of the MFLFM were simulated from a commonly used light field software [17] by additionally adding a grating pattern function for the MFG into the PSF generation model [18]. The simulation parameters of a microscope were the same as those used in the MFLFM experiment as described in section 3.1: $NA = 1.27$, magnification $M = 120$, and lenslet spacing $d = 150 \mu\text{m}$. The number of pixel behind each lenslet was $N_u \times N_v = 11 \times 11$, which gave a pixel size of $0.1136 \mu\text{m}$ in the object space. The grating pattern function for the MFG was generated

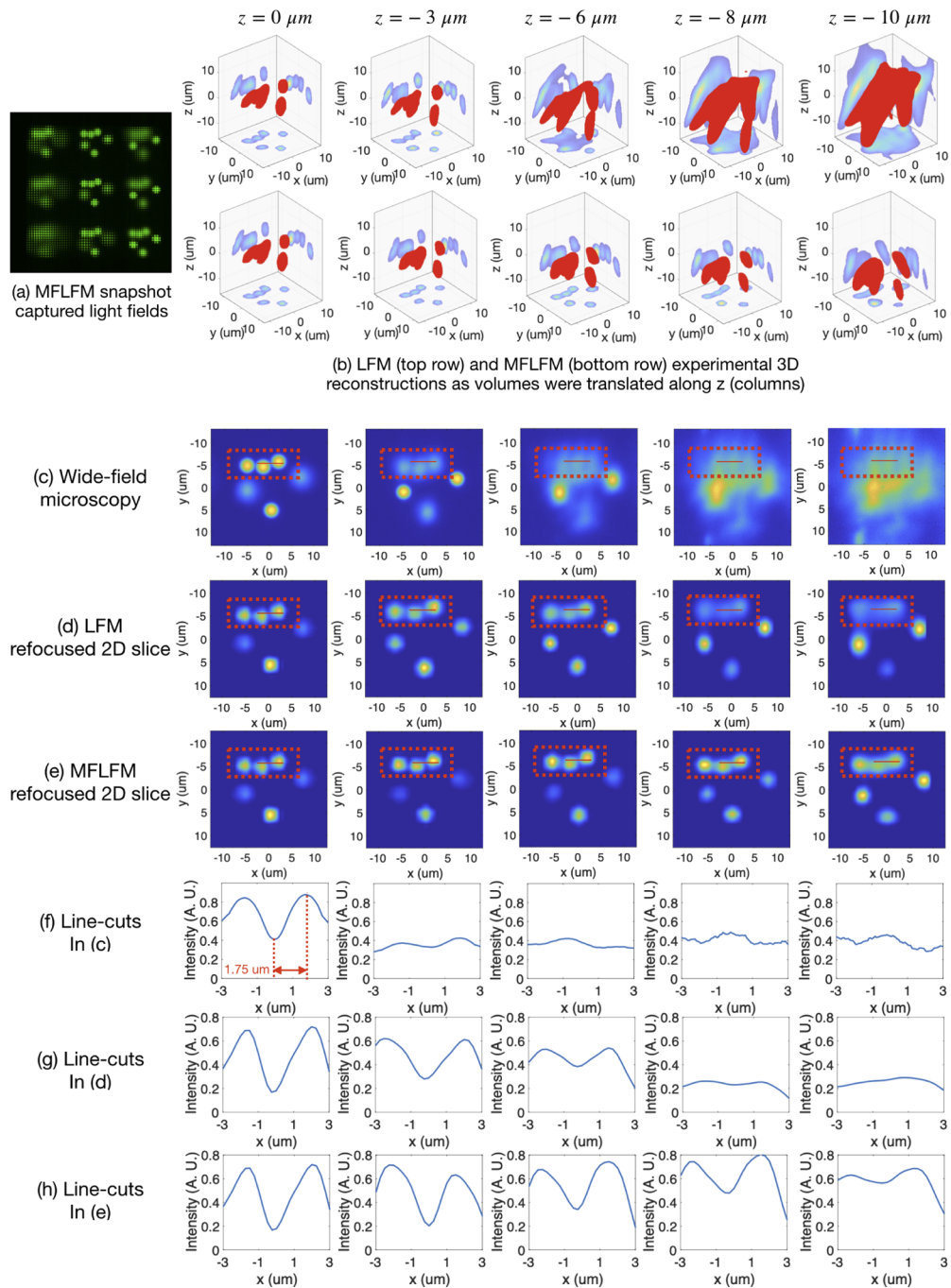


Fig. 6. The MFLFM proof-of-principle experimental results and quantitative analysis. (a) A snapshot captured MFLFM light fields measurement. (b) The light field 3D reconstructions for the LFM (top row) and MFLFM (bottom row) using synthetic focusing algorithms. Each column shows reconstructions of the 3D volume as it was translated to the different z -heights denoted above each image. (c) Wide-field microscopy images when three beads outlined in a red dash rectangle were in focus (first column) and out-of-focus (second to last columns). (d) The LFM and (e) MFLFM refocused 2D slice of the three beads. (f-h) Linecuts comparisons indicated by red solid lines in (c-e), respectively. The beads could not be resolved by the LFM when it refocused at z -position larger than $6 \mu\text{m}$, but could be well separated by the proposed MFLFM even it refocused at $z = -10 \mu\text{m}$, demonstrating that the MFLFM could extend the DOF of the LFM without sacrificing its spatial lateral resolution.

from a grating design process [16]. The simulated MFLFM PSF (690×690 pixels) consisting of 3×3 differently focal shifted light fields is shown in Fig. 7(b). The MFLFM measurement (shown in Fig. 7(c)) was computed from the forward model of Eq. (3), and then corrupted by the Poisson noise. Here, we assumed 10 photons per pixel on average. For the comparison, we also simulated a conventional microscope and a LFM with the same imaging parameters and total photon budget.

Figure 8 shows the deconvolution reconstructions for the conventional microscope (a), LFM (b) and MFLFM (c) respectively as the resolution test target was moved to different z -positions denoted above each image (columns). To quantify the lateral resolution across depth, the linecuts comparisons indicated by blue line in both LFM and MFLMF were plotted in Fig. 8(d) and 8(e), respectively. As expected, a conventional microscope [Fig. 8(a)] produced the best resolution at the native focal plane ($z = 0$). But it suffered from a shallow DOE and the lateral resolution degraded quickly as it went out-of-focus (from second column to the last). The LFM [Fig. 8(b)] extended the DOF of the conventional microscope. However, the lateral resolution of the light field reconstruction was not uniform within the DOF. For example, from Fig. 8(d) one can see that the LFM could not resolve the three horizontal lines with a vertical spacing of $0.68 \mu\text{m}$ except at $z = 1 \mu\text{m}$ depth. On the other hand, in the MFLFM light field deconvolution [Fig. 8(e)], those three lines were well separated by a dip of 28% on average within the whole DOF from $z = 0 \mu\text{m}$ to $z = 5 \mu\text{m}$. Peak signal-to-noise ratio (PSNR) and the structural similarity index (SSIM) of the reconstructed images [shown in Figs. 8(b) and (c)] were also computed in Fig. 9. Those plots also clearly demonstrated that the low image reconstruction quality at both the native focal plane and increasing z depths in the LFM were improved significantly by the MFLFM.

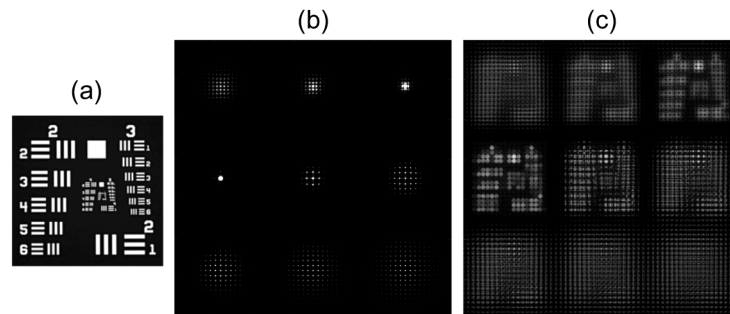


Fig. 7. (a) Ground truth image of a USAF 1951 resolution target, (b) simulated MFLFM PSF and (c) simulated MFLFM image under Poisson noise corruption.

Finally, we investigated the impact of signal-to-noise ratio (SNR) on the light field deconvolution reconstructions for both LFM and MFLFM by repeating the simulation with different photon budgets. To this end, here, we specified varying average numbers of photons per pixel for each simulation (i.e., 1 photon/pixel, 2 photons/pixel, 5 photons/pixel etc). The total photon budget was therefore a product of the number of the pixels and the average number of photon per pixel. For fair comparisons, we assumed that the total photon budget was same for both systems. Due to light splitting and a 68% diffraction efficiency of the MFG in the MFLFM, the average photon collected per pixel in the light field of the MFLFM system was about 20 ($690^2/187^2/0.68 = 20$) times less than that of the LFM. The PSNR and SSIM of light field deconvolution reconstructions under different numbers of photon collected per pixel (colors) for both LFM (dash lines) and MFLFM (solid lines) were plotted in Fig. 10. We can see that the proposed MFLFM was able to produce a higher and more uniform lateral resolution across depth than the LFM under the same photon budget.

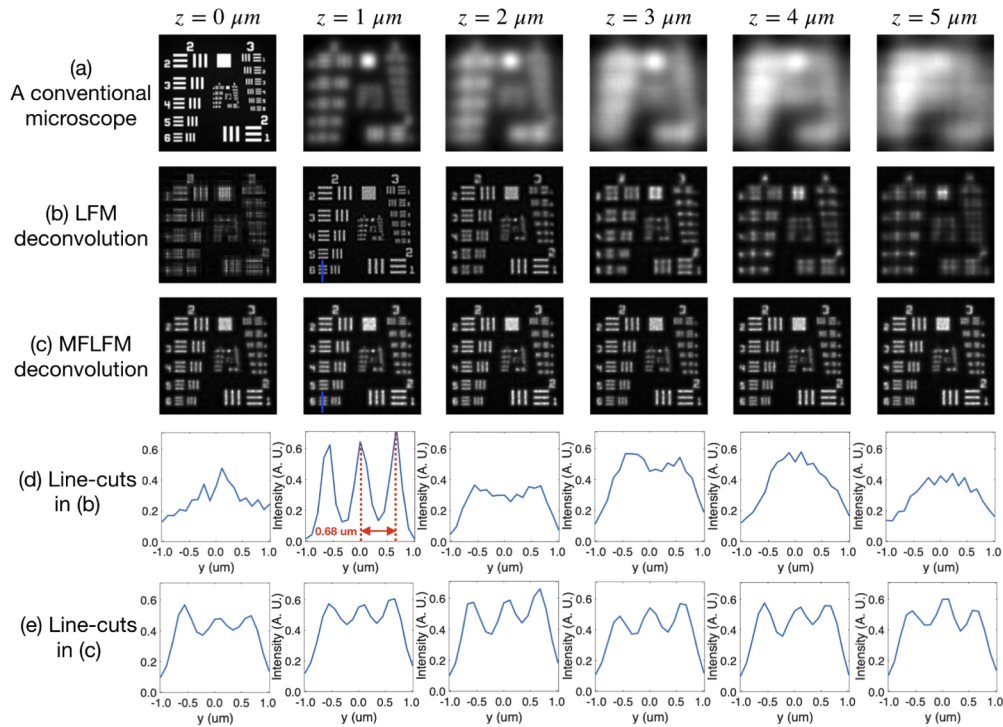


Fig. 8. Simulation results: deconvolution reconstructions for (a) a conventional wide-field microscope, (b) the LFM, and (c) proposed MFLFM as a USAF 1951 resolution test target was moved to different z -positions denoted above each image. (d-e) The linecuts comparisons indicated by blue line in (b) and (c). The three lines with a spacing of about $0.68 \mu\text{m}$ could not be distinguished by the LFM (d) except at $z = 1 \mu\text{m}$ depth but could be super resolved within the whole DOF in the MFLFM.

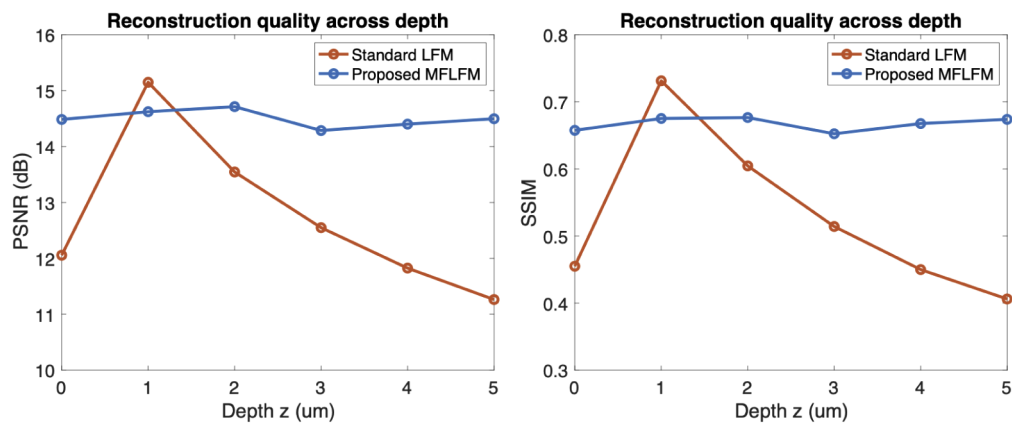


Fig. 9. PSNR (left) and SSIM (right) of the LFM (red) and MFLFM (blue) reconstructed images shown in Figs. 8(b) and (c). The low uniformity of reconstruction quality in the LFM was significantly improved by the proposed MFLFM method.

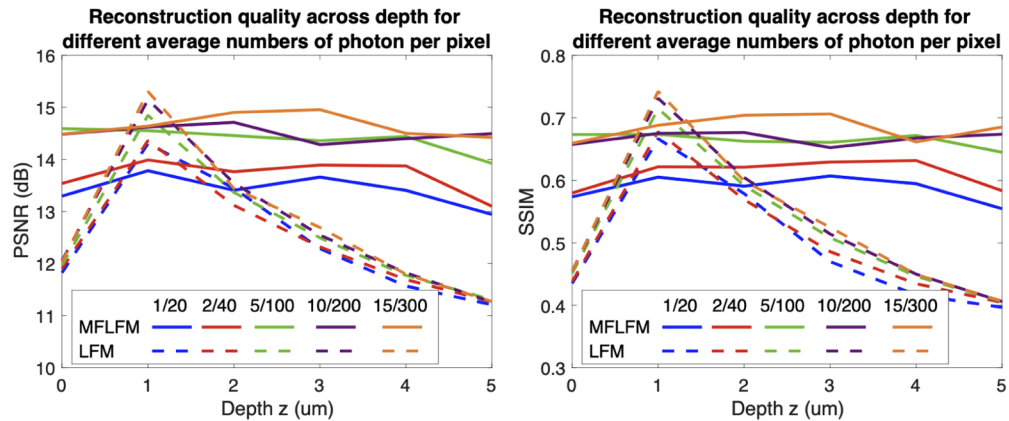


Fig. 10. Impact of signal-to-noise ratio on the light field reconstructions for the LFM (dash lines) and MFLFM (solid lines). The colors of lines denote different numbers of photon collected per pixel. Here, the format $n1/n2$ in the legend denotes $n1$ and $n2$ average photon per pixel for the MFLFM and LFM, respectively, to ensure the same total photon budget for both imaging systems.

4. Conclusion and discussion

In this paper, we have proposed a novel multifocal light field microscopy (MFLFM). We presented an MFLFM prototype system by placing a multifocus grating in the Fourier plane of a conventional LFM. We showed that the MFLFM was able to collect 9 focal shifted light fields in a snapshot shot without a need for focal scanning. We analyzed the DOF and theoretical lateral resolution limits for the MFLFM. We experimentally demonstrated a $8 \mu\text{m}$ DOF improvement of the MFLFM over the LFM using synthetic focusing algorithms for the light field reconstruction. We also presented simulation results and performed quantitative resolution analysis to show that the MFLFM was able to achieve uniform lateral resolution across depth in the light field deconvolution, overcoming the non-uniform resolution problem of the LFM.

It's worth discussing the trade-offs of the conventional LFM and the MFLFM approaches. In a conventional LFM design, the space-bandwidth product (SBP) is divided between angular and lateral spatial resolution, which can significantly reduce the maximum spatial resolution achieved. However, this loss can be significantly mitigated by utilizing optimization algorithms incorporating wave optics modeling of the LFM instrument. For instance, the authors of [4] demonstrated a super-resolution reconstruction beyond the lenslet spatial sampling rate in the LFM by using deconvolution algorithms. While the lateral resolution for some depths was improved significantly using deconvolution, it was not improved in the focal plane of the sensor. Because our MFLFM uses the same wave-optics deconvolution approach as [4], it significantly increases lateral resolution relative to conventional LFM (see Figs. 8 and 9). However, our MFLFM approach sacrifices lateral FOV to computationally increase DOF. This increase in DOF is achieved while also maintaining high lateral resolution via a 3D deconvolution reconstruction. Furthermore, while 3D deconvolution methods applied to conventional LFM suffer from extremely poor lateral resolution in the focal plane of the LFM sensor, our MFLFM does not. The sacrificed lateral FOV in the MFLFM could be circumvented by splitting the optical path with beam-splitters and imaging with multiple MLAs and sensors focused on different z -positions in the volume. In this case, each light field has a full sensor FOV. Our analysis and conclusions on the DOF extension and lateral resolution improvement presented in this paper are applicable to both systems.

Funding

National Science Foundation (IIS-1453192); U.S. Department of Energy (DE-AC02-06CH11357).

Disclosures

The authors declare no conflicts of interest.

References

1. M. Levoy, R. Ng, A. Adams, M. Footer, and M. Horowitz, "Light field microscopy," *ACM Trans. Graph.* **25**(3), 924–934 (2006).
2. R. Ng, "Fourier slice photography," in *Proceedings of the International Conference on Computer Graphics and Interactive Techniques (SIGGRAPH'05)*, (2005), pp. 735–744.
3. R. Ng, M. Levoy, M. Br, G. Duval, M. Horowitz, P. Hanrahan, and D. Design, "Light field photography with a hand-held plenoptic camera," (2005).
4. M. Broxton, L. Grosenick, S. Yang, N. Cohen, A. Andalman, K. Deisseroth, and M. Levoy, "Wave optics theory and 3-d deconvolution for the light field microscope," *Opt. Express* **21**(21), 25418–25439 (2013).
5. M. Alam and B. Gunturk, "Hybrid light field imaging for improved spatial resolution and depth range," *Mach. Vis. Appl.* **29**(1), 11–22 (2018).
6. J.-S. Jang and B. Javidi, "Large depth-of-focus time-multiplexed three-dimensional integral imaging by use of lenslets with nonuniform focal lengths and aperturesizes," *Opt. Lett.* **28**(20), 1924–1926 (2003).
7. T. Georgiev and A. Lumsdaine, "The multi-focus plenoptic camera," *Proc. SPIE* **8299**, 829908 (2012).
8. N. Cohen, S. Yang, A. Andalman, M. Broxton, L. Grosenick, K. Deisseroth, M. Horowitz, and M. Levoy, "Enhancing the performance of the light field microscope using wavefront coding," *Opt. Express* **22**(20), 24817–24839 (2014).
9. P. Prabhat, S. Ram, E. Ward, and R. Ober, "Simultaneous imaging of different focal planes in fluorescence microscopy for the study of cellular dynamics in three dimensions," *IEEE Trans.on Nanobioscience* **3**(4), 237–242 (2004).
10. S. Ram, P. Prabhat, J. Chao, E. Ward, and R. Ober, "High accuracy 3d quantum dot tracking with multifocal plane microscopy for the study of fast intracellular dynamics in live cells," *Biophys. J.* **95**(12), 6025–6043 (2008).
11. D. Kim, R. Ober, S. Ram, and E. Ward, "3d single molecule tracking of rapid intracellular trafficking imaged by multifocal plane microscopy," *Microsc. Microanal.* **18**(S2), 146–147 (2012).
12. S. Abrahamsson, B. H. J. Chen, S. Stallinga, A. Y. Katsov, J. Wisniewski, G. Mizuguchi, P. Soule, F. Mueller, C. D. Darzacq, X. Darzacq, C. Wu, C. I. Bargmann, D. A. Agard, M. Dahan, and M. G. L. Gustafsson, "Fast multicolor 3d imaging using aberration-corrected multifocus microscopy," *Nat. Methods* **10**(1), 60–63 (2013).
13. K. He, Z. Wang, X. Huang, X. Wang, S. Yoo, P. Ruiz, I. Gdor, A. Selewa, N. J. Ferrier, N. Scherer, M. Hereld, A. K. Katsaggelos, and O. Cossairt, "Computational multifocal microscopy," *Biomed. Opt. Express* **9**(12), 6477–6496 (2018).
14. S. Abrahamsson, R. Ilic, J. Wisniewski, B. Mehl, L. Yu, L. Chen, M. Davanco, L. Oudjedi, J.-B. Fiche, B. Hajj, X. Jin, J. Pulupa, C. Cho, M. Mir, M. E. Beheiry, X. Darzacq, M. Nollmann, M. Dahan, C. Wu, T. Lionnet, J. A. Liddle, and C. I. Bargmann, "Multifocus microscopy with precise color multi-phase diffractive optics applied in functional neuronal imaging," *Biomed. Opt. Express* **7**(3), 855–869 (2016).
15. B. Hajj, L. Oudjedi, J.-B. Fiche, M. Dahan, and M. Nollmann, "Highly efficient multicolor multifocus microscopy by optimal design of diffraction binary gratings," *Sci. Rep.* **7**(1), 5284 (2017).
16. S. Abrahamsson, M. McQuilken, S. B. Mehta, A. Verma, J. Larsch, R. Ilic, R. Heintzmann, C. I. Bargmann, A. S. Gladfelter, and R. Oldenbourg, "Multifocus polarization microscope (mf-polscope) for 3d polarization imaging of up to 25 focal planes simultaneously," *Opt. Express* **23**(6), 7734–7754 (2015).
17. R. Prevedel, Y.-G. Yoon, M. Hoffmann, N. Pak, G. Wetzstein, S. Kato, T. Schrödel, R. Raskar, M. Zimmer, E. S. Boyden, and A. Vaziri, "Simultaneous whole-animal 3d imaging of neuronal activity using light-field microscopy," *Nat. Methods* **11**(7), 727–730 (2014).
18. K. He, X. Huang, X. Wang, S. Yoo, P. Ruiz, I. Gdor, N. J. Ferrier, N. Scherer, M. Hereld, A. K. Katsaggelos, and O. Cossairt, "Design and simulation of a snapshot multi-focal interferometric microscope," *Opt. Express* **26**(21), 27381–27402 (2018).